Wide domain simulations of flow over an unswept laminar wing section undergoing transonic buffet

Markus Zauner[*]
Aerodynamics Aeroelasticity Acoustics Department, ONERA - The French Aerospace Lab, Meudon 92190, France

Neil D. Sandham[†]
Aerodynamics and Flight Mechanics Group, University of Southampton, Southampton SO17 1BJ, United Kingdom

(Received 30 April 2020; accepted 24 July 2020; published 20 August 2020)

Transonic buffet is an unsteady flow phenomenon that limits the safe flight envelope of modern aircraft. Scale-resolving simulations with span-periodic boundary conditions can provide detailed insight into the flow physics associated with buffet and can help to calibrate simplified models that are needed, for example, to develop more efficient wings based on laminar-flow supercritical sections. However, such simulations are often feasible only for severely restricted spanwise domains. In the current contribution, we analyze an unswept laminar-flow wing section (of Dassault Aviation's V2C profile) at a moderate Reynolds number of $\mathrm{Re} = 500\,000$ and a Mach number of $M = 0.7$ with spanwise domains equal to 5% and 100% of the airfoil chord. An implicit large-eddy simulation methodology, using a spectral error estimator to control the action of a high-order filter, is first validated against direct numerical simulations and then used for the domain width study. Quantitative differences, due to domain size, include an increase in amplitude and regularity of the buffet oscillations in the wider domain. Nevertheless, a space-time analysis shows that key physical phenomena such as upstream-propagating shock waves are properly represented in the narrow domain and there is limited sensitivity to the domain size of the aerodynamic coefficients. Even in the very wide domain, which is an order of magnitude wider than the largest turbulent structures measured at the trailing edge, certain features remain two dimensional, including the shock and expansion waves that interact with the boundary layer upstream of transition. The transition mechanism is found to have subtle variations during a typical buffet cycle, with Kelvin-Helmholtz structures prominent during low-lift phases and oblique modes developing behind shock/boundary-layer interactions during high-lift phases. The availability of the wide domain data is used for further study of the buffet mechanism, considering phase-averaged data and instantaneous flow fields to show the global structure of the buffet oscillation.

DOI: 10.1103/PhysRevFluids.5.083903

I. INTRODUCTION

Transonic buffet is usually associated with large-amplitude, autonomous shock oscillations, caused by the interactions between shock waves and separated shear layers, for which there is a

[*]Also at Aerodynamics and Flight Mechanics Group, University of Southampton, Southampton SO17 1BJ, United Kingdom; mzauner@onera.fr
[†]n.sandham@soton.ac.uk

substantial literature base [1–4]. Different types of shock motion (back and forth moving shocks or periodically upstream-propagating shock waves) have been studied by Ref. [5] and have also been reported for several rigid airfoils under buffet conditions [6–9]. The structural response of wings and control surfaces to these aerodynamic oscillations is commonly referred to as "buffeting," which limits the safe flight envelope of modern aircraft. Therefore, it is of great interest to be able to predict buffet onset as precisely as possible. While traditional explanations for transonic buffet (e.g., acoustic feedback and wave-propagation models [8,10–14]) have difficulties to directly couple the shock motion with the low-frequency fluctuations in the lift [15–17], more recent studies describe transonic buffet as a global instability [18–20].

Buffet has some different characteristics on swept versus unswept wings. While for unswept cases, transonic buffet is associated with a sharp spectral peak at Strouhal numbers (defined as $\mathrm{St} = fc/U_\infty$) in the range of $\mathrm{St} \approx 0.05$–0.1, a broadband frequency signature exists for swept-wing cases. Furthermore, chordwise shock oscillations are more confined in the swept cases with variations in the spanwise direction. Outboard-traveling shock waves can also be connected to so-called "buffet cells" [21–23]. Not everything is different, however, since recent studies for swept wings also exhibit a sharp spectral peak comparable to unswept cases [24], where the mode associated with the broadband swept-wing behavior seems to be driven by flow-separation phenomena and converges towards a zero-frequency mode for decreasing sweep angles [25]. These results suggest that there is more to learn from unswept cases, as they not only capture phenomena that are still not fully understood, but are connected to more general swept-wing configurations.

So far, airfoils and wing sections with mainly turbulent boundary layers have dominated transonic buffet research. However, challenging emission goals have encouraged research into laminar-flow designs with potential fuel savings of the order of 10% for typical commercial aircraft. The key to this technology is to maintain laminar boundary layers over a large part of the airfoil in order to reduce skin-friction drag, even though laminar boundary layers can be more sensitive to disturbances and off-design conditions. To exploit its full potential it is important to understand and eventually to be able to control key flow phenomena such as laminar shock-wave/boundary-layer interaction and undesired instabilities such as transonic buffet. Experimental studies have reported significant differences in the buffet characteristics under laminar-flow conditions. For an RA16 airfoil with a natural transition ($\mathrm{Re} = 3$–6×10^6), Ref. [26] reported a strong increase of the pressure fluctuation level without any particular frequency, instead of the typical sharp spectral peak [27]. Also, Ref. [28] compared laminar and turbulent buffet characteristics of an OAT15A airfoil and for the laminar case found a dominant peak at significantly higher frequencies ($\mathrm{St} \approx 0.9$) compared to the turbulent case ($\mathrm{St} \approx 0.06$). Numerical studies have recently been applied to laminar-flow airfoils. Analyzing ONERA's OALT25 profile using large-eddy simulations, Ref. [29] reported a sharp spectral peak at significantly higher frequencies ($\mathrm{St} = 1.2$ instead of $\mathrm{St} = 0.06$) and more confined shock motion compared to a case with tripped boundary layers. Experimental investigations on the same airfoil also reported this sharp peak at $\mathrm{St} = 1.2$, but with a less dominant broadband phenomenon at $\mathrm{St} \approx 0.05$ [30]. Analyses of Dassault Aviation's laminar-flow V2C profile showed a quite different trend, as Strouhal numbers were reported in the range of $\mathrm{St} = 0.12$–0.16 for laminar as well as for tripped turbulent cases, albeit different from typical Strouhal numbers mentioned above. This airfoil geometry was the subject of experimental [31,32] as well as numerical studies [33–36] and is also considered for our investigations. It is likely that, over some parameter ranges and airfoil geometries, different types of buffet exist (or can even coexist) [16,30,37] and it is still unclear how they relate to each other and to turbulent cases [38].

Further progress to clarify the mechanisms can be made using scale-resolving simulations. However, due to the high resolution of direct numerical simulations (DNSs) that is required even at moderate Reynolds numbers (for example, grid spacings based on wall scaling of $\Delta x^+ < 5$, $\Delta y^+ < 1$, $\Delta z^+ < 5$ [37,39]), both the runtime and domain width have been limited. For example, the grid required for a well-resolved DNS at moderate Reynolds numbers considering a narrow domain of 5% of the chord length contains approximately 1 billion grid points and required more

than 130 000 core hours to compute one dimensionless time unit, which is defined as the ratio of chord length and free-stream velocity (c/U_∞), making parametric studies unfeasible.

Large-eddy simulations (LESs) have the potential to capture the main flow phenomena involved in buffet, saving several orders of magnitude in cost versus DNS. Previous scale-resolving simulations of airfoils at transonic buffet conditions have captured the low-frequency unsteadiness [37,40,41], but have also recognized the sensitivity to the computational grid and subgrid scale model [36,40], which becomes even more of a challenge when details of the transition process must be captured [42]. The particular challenges include the need for stretched, curvilinear grids and the presence of significant portions of a laminar boundary layer where any subgrid model must turn off to avoid unphysical additional dissipation. In order to maintain the numerical stability of LESs with subgrid models, however, filtering is often required, and in an airfoil flow the amount of filtering necessary may be different within the boundary layer as opposed to the near acoustic field. Implicit LESs (ILESs) can be attractive, since in this kind of flow one already has schemes designed for adding dissipation to capture shock waves without spurious oscillations [43]. However, without additional tuning, ILES can also be far too dissipative in key regions with transitional or turbulent flow features [44]. In this context, one aspect of the current work is to try to improve methods for airfoil flow and here we use a technique that is highly selective in where filtering is applied. In addition to shock capturing, which is carefully limited to the immediate vicinity of shock waves using a proven methodology, we also control filtering away from shocks, where mostly we are relying on central difference schemes that develop oscillations when the flow is underresolved. The methodology adopted here is to detect these characteristic oscillations and apply local filtering, helping to minimize the amount of filtering. The method will be validated against DNS for a buffet test case. Eventually, the data of such benchmark cases can be used to improve turbulence and transition models in order to facilitate more efficient simulation methods [e.g., unsteady Reynolds-averaged Navier-Stokes (URANS)] with increased complexity of the test case (e.g., half-wing configuration, fluid/structure interaction, etc.).

The main objective of the present contribution is to assess the influence of the spanwise domain size on key physical phenomena associated with buffet. If key phenomena are captured in the narrower domain, this justifies its use for further fundamental studies including instability analyses. If significant differences are found, then we know that we need to use the wider domains. To check the effects, we run two cases with a factor of 20 different spanwise domain size. In Sec. II we describe the spectral-error-based implicit large-eddy simulation (SE-ILES) methodology, which is validated against DNS in Sec. III, demonstrating excellent results with a factor of 16 overall saving in computer time relative to the DNS. In Sec. IV we make the central comparison of domain size using aerodynamic coefficients, x/t diagrams, and two-point correlations. In Sec. V we exploit the data from the wide domain size to study the transition and low-frequency phenomena in more detail and make conclusions in Sec. VI.

II. METHODOLOGY

All simulations reported here were carried out using the high-order parallel multiblock finite-difference in-house code SBLI. Details of the solver and previous applications can be found in Refs. [45–47]. The basic setup outlined in this section is the same as the direct numerical simulations in Ref. [37]. The dimensionless time-dependent compressible Navier-Stokes equations in three spatial dimensions can be written as

$$\frac{\partial \rho}{\partial t} + \frac{\partial \rho u_i}{\partial x_i} = 0, \tag{1}$$

$$\frac{\partial \rho u_i}{\partial t} + \frac{\partial \rho u_i u_j}{\partial x_j} = -\frac{\partial p}{\partial x_i} + \frac{1}{\mathrm{Re}} \frac{\partial \tau_{ij}}{\partial x_j}, \tag{2}$$

$$\frac{\partial E_t}{\partial t} + \frac{\partial E_t u_j}{\partial x_j} = -\frac{\partial p u_j}{\partial x_j} + \frac{\partial q_j}{\partial x_j} + \frac{1}{\mathrm{Re}} \frac{\partial (u_i \tau_{ij})}{\partial x_j}. \tag{3}$$

The pressure and heat flux are denoted by p and Q, respectively, while τ denotes the stress tensor. The nondimensionalization scheme used to formulate the above equations is based on the free-stream density ρ^*_∞, velocity u^*_∞, and temperature T^*_∞, where the asterisk denotes dimensional quantities. The pressure p is normalized by $\rho^*_\infty u^{*2}_\infty$. The characteristic length is set according to the airfoil chord length c. The five conservative variables are contained in a solution vector q, consisting of the density ρ, the specific momentum components ρu, ρv, and ρw, and the volume specific total energy $E_t = \rho e_{\text{int}} + 1/2 \times \rho(uu + vv + ww)$, where $e_{\text{int}} = T/[\gamma(\gamma - 1)M^2]$ denotes the specific internal energy. The fluid is considered as a Newtonian fluid with the stress tensor

$$\tau_{ij} = \mu\left(\frac{\partial u_i}{\partial x_j} + \frac{\partial u_j}{\partial x_i} - \frac{2}{3}\frac{\partial u_k}{\partial x_k}\delta_{ij}\right), \tag{4}$$

where μ and δ_{ij} denote the kinematic viscosity and the Kronecker delta, respectively. The heat conduction is considered according to Fourier's law, written in dimensionless form as

$$q_j = -\frac{\mu}{(\gamma - 1)\text{Re}\,\text{Pr}\,M^2}\frac{\partial T}{\partial x_j}, \tag{5}$$

where the specific heat ratio and Prandtl number are assumed to be constant with $\gamma = 1.4$ and $\text{Pr} = 0.72$, respectively.

The temperature dependency of the dynamic viscosity is modeled by Sutherland's law according to

$$\mu = T^{\frac{3}{2}}\frac{1 + C_{\text{Suth}}}{T + C_{\text{Suth}}}, \tag{6}$$

where the Sutherland constant is set to $C_{\text{Suth}} = 110.4/T^*_\infty = 0.41$ with $T^*_\infty = 268.67$ K. For statistical analysis, the Favre (density weighted) average of a variable q is defined by

$$\tilde{q} = \frac{\overline{\rho q}}{\overline{\rho}}, \tag{7}$$

where an overbar denotes the usual Reynolds average.

The equations are discretized in time using an explicit third-order low-storage Runge-Kutta scheme and in space by applying a fourth-order central finite-difference scheme on a structured multiblock grid. Five-point stencils are used to calculate the interior of the flow field, while the boundaries are treated by a fourth-order accurate scheme according to Ref. [48]. The same discretization schemes were used for DNSs of airfoil flows by Ref. [47]. Figure 1(a) shows an LES grid (every 18th and 14th grid point in the ξ and η direction, respectively) and Fig. 1(b) a closeup of the airfoil (details Ⓟ and Ⓑ will be explained later). Zonal characteristic boundary conditions [49] are applied at the outlet [highlighted with green in Fig. 1(a)], whereas integral characteristic boundary conditions [50] are applied at the remaining outer boundaries (highlighted in orange). Due to the appearance of shock waves, a total variation diminishing (TVD) scheme is used, but limited to the immediate vicinity of shock waves and turned off completely within a small zone near the leading edge, as described in Ref. [37]. To avoid the formation of spurious structures in the free stream, a sixth-order filter, similar to the one used by Ref. [51], is incorporated in the far field, but disabled within a distance of $\Delta n \approx 0.2$ from the airfoil surface (the boundary is sketched by the magenta lines), so that the boundary layer and near-wake flow features are not affected. For the filtering, we solve the tridiagonal system

$$\alpha_f \breve{q}_{(i-1)} + \breve{q}_i + \alpha_f \breve{q}_{(i+1)} = \sum_{n=0}^{N}\frac{a_n}{2}(q_{(i+n)} + q_{(i-n)}) \quad \text{with } N = 3, \tag{8}$$

where q and $\breve{q}$ denote unfiltered and filtered components of the solution matrix, respectively. The adjustable parameter is set to $\alpha_f = 0.45$, while the coefficients are derived in terms of α_f using

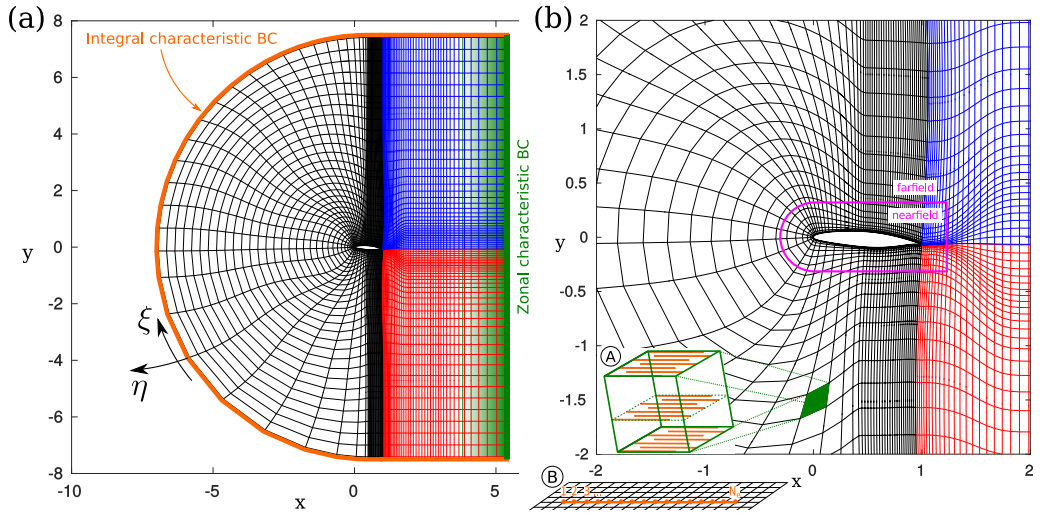

FIG. 1. (a) Multiblock LES grid plotting every 18th and 14th grid point in the ξ and η direction, respectively. Integral characteristic and zonal characteristic boundaries are highlighted in orange and green, respectively. (b) Closeup of the region around the airfoil, where the magenta lines sketch the boundary between the near and far field. Details Ⓐ and Ⓑ indicate a processor block and a stencil for error-indicator calculation, respectively.

Taylor- and Fourier-series analyses [51] as

$$a_0 = \frac{11}{16} + \frac{5\alpha_f}{8}, \quad a_1 = \frac{15}{32} + \frac{17\alpha_f}{16}, \quad a_2 = \frac{-3}{16} + \frac{3\alpha_f}{8}, \quad a_3 = \frac{1}{32} + \frac{1\alpha_f}{16}. \tag{9}$$

References [52,53] provide more detailed information on the filtering technique. The filter is applied to the conserved variables in each spatial direction in a sequential way. In the current implementation, an additional coefficient a_{lim} is specified according to the update algorithm

$$q_{\text{new}} = q_{\text{orig}} - a_{\text{lim}} \cdot (q_{\text{orig}} - \breve{q}), \tag{10}$$

where q_{orig} is the solution before applying the filter and q_{new} contains the updated variable. For direct numerical simulations, a_{lim} is set to $a_{\text{lim}} = 0.1$ in the free-stream region, where the filter is applied. This approach has also been used to improve the numerical stability of simulations with decreased resolutions, for example, during initial grid studies. More details on the numerical implementation are provided in Ref. [37].

The present contribution utilizes a newly developed spectral-error-based implicit large-eddy simulation (denoted SE-ILES) approach, which uses the same sixth-order filter as used in the free stream, but with the filter coefficient set to $a_{\text{lim}} = 0.4$. In the SE-ILES approach, this filter is only applied in regions that are developing grid-to-grid point oscillations, and hence does not affect structures in well-resolved regions. Corresponding to the number of available computational cores, the domain is split into subdomains, here denoted as processor blocks (PBs), so that each core solves the flow for approximately the same number of grid points. In the present case, each three-dimensional PB contains approximately ∼25 000 grid points [∼2500 grid points in the two-dimensional (2D) plane] and sketched by the green box (detail Ⓐ) in Fig. 1(b). To identify insufficiently resolved regions of the flow we adopt a spectral error estimator previously used to identify regions of poor resolution and then for iterative grid design [54,55]. For fully developed turbulence we expect the energy in small-scale structures to reduce with increasing wave number according to Kolmogorov's $-5/3$ law in the inertial sublayer, or at an even higher rate in the dissipation range. However, for high-order finite-difference schemes, we often observe significantly

weaker decay rates, or even spectra that increase with increasing wave number, in regions of reduced grid resolution. Spectral error indicators are used to efficiently estimate the actual spectral decay rate against a specified minimum acceptable decay rate. Explicit filtering is then applied only in regions with high error severity. Spectral error indicators are also applied in the context of spectral element simulations of wing flows to control grid adaptation [56].

In the present approach, spectral error indicators are calculated every $N_E = 10$ time steps for each processor block according to Ref. [54] using the vorticity magnitude $|\omega|$. Instead of computing the full spectra for each 3D PB, the Fourier amplitudes A_2, A_4, and A_8 (proportional to the square root of the spectral energy) of selected modes $(N_e/2, N_e/4, N_e/8)$ for stencils of $N_e = 16$ grid points [detail Ⓑ in Fig. 1(b)] are defined by

$$A_2 = \frac{2^{-2r}}{N_e}\sum_{j=0}^{N_e-1}(-1)^j|\omega_j|, \quad A_4 = \frac{2^{1-r}}{N_e}\sum_{j=0}^{N_e-1}(-i)^j|\omega_j|, \quad A_8 = \frac{2}{N_e}\sum_{j=0}^{N_e-1}\exp\left(-\frac{\pi}{4}i\right)^j|\omega_j|. \tag{11}$$

The parameter r denotes the minimum acceptable decay rate of amplitudes in the short-wavelength part of the spectrum, here set to $r = -1$. The average of Fourier amplitudes $(\overline{A})$ of a set of similarly oriented stencils, which are homogeneously distributed within the PB [indicated by the staggered orange lines for representative planes in detail Ⓐ of Fig. 1(b)], is calculated and the mean error indicator $\overline{I_f}$ is obtained by

$$\overline{I_f} = \ln\left(1 + \left\lfloor\frac{\overline{A_2}}{\overline{A_4}+\epsilon}\right\rfloor + \left\lfloor\frac{\overline{A_4}}{\overline{A_8}+\epsilon}\right\rfloor + \left\lfloor\frac{\overline{A_2}}{\overline{A_8}+\epsilon}\right\rfloor\right), \tag{12}$$

with

$$\overline{A_2} = \sum_{n=1}^{N_{\text{stencil}}}\frac{A_{2,n}}{N_{\text{stencil}}}, \quad \overline{A_4} = \sum_{n=1}^{N_{\text{stencil}}}\frac{A_{4,n}}{N_{\text{stencil}}}, \quad \text{and} \quad \overline{A_8} = \sum_{n=1}^{N_{\text{stencil}}}\frac{A_{8,n}}{N_{\text{stencil}}}, \tag{13}$$

where $\lfloor\cdots\rfloor$ is a "floor" operation and $\epsilon = 0.03$ used to avoid division by zero and tune the error-indicator sensitivity [54]. In cases where $\overline{I_f}$ exceeds a value of $\varepsilon_1 = 0.6$, the error in this PB is considered as high. The threshold is based on a grid study of the Taylor-Green vortex test case [54]. In addition to the instantaneous error, an average error is computed according to

$$\varepsilon_{\text{av}} = (1 - C_{\text{av}})\varepsilon_{\text{av}} + C_{\text{av}} \quad \text{if } \overline{I_f} > \varepsilon_1, \tag{14}$$

$$\varepsilon_{\text{av}} = (1 - C_{\text{av}})\varepsilon_{\text{av}} + C_{\text{av}}\frac{N_{\text{high}}}{N_{\text{check}}} \quad \text{else}, \tag{15}$$

which indicates the probability of $\overline{I_f}$ exceeding the threshold ε_1 in this PB using $C_{\text{av}} = 0.1$. The number of cases in which spectral errors were calculated and exceeded the threshold ε_1 is denoted by N_{high}, while N_{check} denotes the total number of checks.

Every $N_F = 30$ time steps, the filter is applied in a PB, if either $\overline{I_f} > \varepsilon_1$ or $\varepsilon_{\text{av}} > \varepsilon_2$ (for the present study $\varepsilon_2 = 0.2$). Blending is used to transition from $a_{\text{lim}} = 0.4$ (in PBs with a high spectral error) to $a_{\text{lim}} = 0.0$ in adjacent PBs with low error estimates. This is repeated for three stencil sets within each PB to calculate error indicators corresponding to the curvilinear coordinates and to apply the filter in each direction independently.

Table I summarizes relevant parameters for the spectral-error-based ILES approach. Parameters r, N_e, ϵ, and ϵ_1 are based on Ref. [54], where these settings were shown to do a good job of capturing grid-to-grid point oscillations. The remaining parameters were tuned in the current work and the methodology is applied throughout the simulations. Calculating spectral errors every $N_E = 10$ time steps corresponding to 3.2×10^{-4} time units was found to be sufficient to gain a good representation of the average error ϵ_{av}, when applying filtering (if required) every $N_F = 30$ time steps. In general, it is recommended to keep $N_E < N_F$ to avoid an underestimation of the errors. The factor N_F was adopted from previous uses of filtering to enhance numerical stability. Factor ϵ_2 depends on N_E, as it

TABLE I. Overview of spectral-error-based filter parameters.

Computation of SE indicators				Control of filter activity			
r	N_e	ϵ	N_E	N_F	a_{lim}	ϵ_1	ϵ_2
−1	16	0.03	10	30	0.4	0.6	0.2

accounts for fluctuating error-indicator values within the filter intervals and can be used to increase the sensitivity. The parameter a_{lim} can be used used to control numerical stability. However, if this parameter becomes too high it is better to adapt the grid resolution instead. More details on spectral error indicators and the chosen settings can be found in Refs. [54,55], respectively.

III. COMPARISON OF NARROW DOMAIN DNS AND LES

To validate the SE-ILES approach, comparisons are made with DNS. The objective is to check that various phenomena associated with buffet can be reproduced using the cheaper approach. This then enables longer run times and simulations with wider domains.

Previous DNSs were reported in Ref. [37]. These were run at a moderate Reynolds number of $\text{Re} = 500\,000$, a Mach number of $M = 0.7$, and an angle of attack of $\alpha = 4^\circ$. An extensive grid study resulted in a choice of a computational grid for this flow configuration with around 1 billion grid points, based on a spanwise domain width equal to 5% of the airfoil chord. Due to the computational cost, only a short run time of four buffet cycles was possible, but this is sufficient to assess the capability of SE-ILES to capture the main phenomena.

A summary of the simulations discussed in this section is given in Table II, listing the angle of attack α, Reynolds number, grid size, spanwise domain extent L_z, number of grid points in the spanwise direction N_z, grid spacing of the smallest cells (Δx_{min} and Δy_{min}), and sixth-order filter activity. In the DNS the filtering is only applied in the far field, where the grid stretching results in underresolved acoustic waves, whereas in the SE-ILES filtering is applied in those blocks where underresolution is detected, as described in the previous section. The DNS was started from a 2D solution at a lower Reynolds number, which was extruded in the spanwise direction. Initial volume forcing similar to Ref. [47] was added to the right-hand side of the momentum equations to introduce a random three-dimensional disturbance at the leading edge for a short time period only, which accelerated the formation of turbulent structures. After self-sustained turbulence was fully developed on both sides of the airfoil, the Reynolds number was increased in a stepwise manner, until the target $\text{Re} = 500\,000$ was reached. To initialize the SE-ILES, a DNS solution taken after a few buffet cycles was interpolated onto the coarser SE-ILES grid. It should be noted that starting a SE-ILES with the same setup from a uniform flow field as an initial condition instead, would still develop the same low-frequency unsteadiness, but would lead to a longer transient of at least two low-frequency cycles.

Figure 2 shows the lift coefficient as a function of time for the DNS (blue curve) and SE-ILES (red curve), both with a spanwise domain extent of 5% of the chord length. Looking at the DNS results, low-frequency fluctuations are observed at a Strouhal number of $\text{St} \approx 0.12$. The amplitude of the C_L oscillation shows some variation, with the last two cycles having larger amplitudes than

TABLE II. Overview of simulations discussed in Sec. III.

Case	Name	α	Re	Grid points	L_z	N_z	Δx_{min}	Δy_{min}	Filter
*A*0	DNS	4°	500×10^3	1.07×10^9	$0.05c$	150	4×10^{-4}	6.8×10^{-5}	Far field
*B*0	SE-ILES	4°	500×10^3	75.3×10^6	$0.05c$	50	1×10^{-3}	1.7×10^{-4}	Targeted

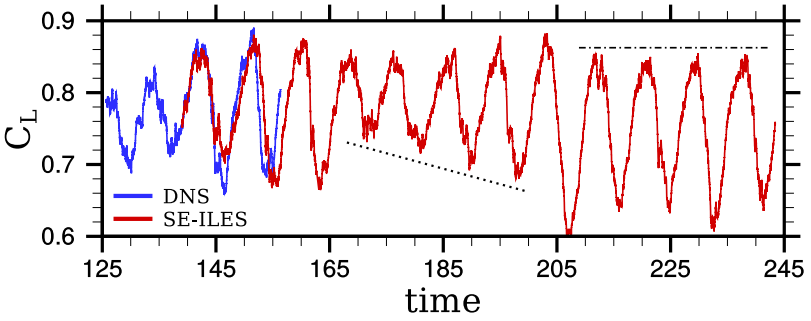

FIG. 2. Instantaneous lift coefficient (of a 2D slice at $z = 0$) of a DNS (blue curve) and SE-ILES (red curve) as a function of time.

the first two. A similar variability can be seen in the SE-ILES results. Shortly after restarting from the DNS solution, the SE-ILES develops a low-frequency phenomenon with similar amplitudes to the DNS. The oscillation is irregular: After approximately 32 time units the minimum lift increases and then steadily decreases again (indicated by the black dotted line). After another four low-frequency cycles, there is a significant drop in the minimum C_L values. The maximum lift over the last four cycles (indicated by the black dashed-dotted line in Fig. 2) is reasonably constant, while the minimum values still show significant variations. Over the full SE-ILES run time the variation of the maxima is only $\Delta C_L \approx 0.03$, while for the minima it is $\Delta C_L \approx 0.14$. The effect of spanwise domain size on this behavior will be shown in the next section. Since a turbulent flow is present, it is expected that the SE-ILES and DNS solutions will eventually diverge from one another. In the context of this paper, the initial agreement between DNS and SE-ILES, with the SE-ILES closely matching the DNS over the first two cycles suggests that the key physical mechanisms resulting buffet are captured in the SE-ILES.

A more detailed comparison of DNS with SE-ILES can be made in the context of x/t diagrams that have been used previously [37] to show the shock and boundary-layer phenomena associated with key frequencies visible in the energy spectra. For orientation, Fig. 3(a) shows an instantaneous 2D slice at $z = 0$ of the streamwise pressure gradient of the DNS at $t = 156.4$. Red contours correspond to compressions, including shock waves, while blue lines indicate expansion regions. It can be seen that a transition to turbulence occurs towards the rear of the airfoil, on both the suction and pressure surfaces, while shock and expansion waves are present upstream, above laminar boundary layers. The white dashed curve, located at a fixed distance ($\Delta n = 0.05c$) from the airfoil surface, is used to monitor and store time-resolved flow-field data, whereas the green lines denote sonic lines ($M = 1$).

Figures 3(b) and 3(c) show contours of the streamwise pressure gradient $\partial p/\partial x$ as a function of space (x) and time (t) for the narrow domain DNS [Fig. 3(b)] and SE-ILES [Fig. 3(c)] along the monitor curve defined in Fig. 3(a). The green lines denote sonic lines and indicate the path of shock waves intersecting the monitor plane. It can be seen that these waves generally move upstream up to about the 30% chord location. The blank region at $t \approx 163$ in Fig. 3(c) is omitted due to corrupted data, but the trends are clear in this region. In addition, the vertical white lines visible near the leading edge are an artifact of the postprocessing which took the closest point to $\Delta n = 0.05$. These lines are less pronounced in Fig. 3(a) due to the increased resolution of the DNS. On the right-hand side of the contour plots, the lift coefficient is shown as a function of time. Representative time segments of SE-ILES and DNS were chosen and synchronized according to their low-frequency cycles. It can be seen that the lift oscillation corresponds to large-scale forward and backward motion of the line of intermittent separation of the boundary layer, which moves forward to 60% chord during the low-lift parts of the cycle and backwards to 70% chord during the high-lift parts of the cycle. The separation is followed by fine lines with positive slope. These

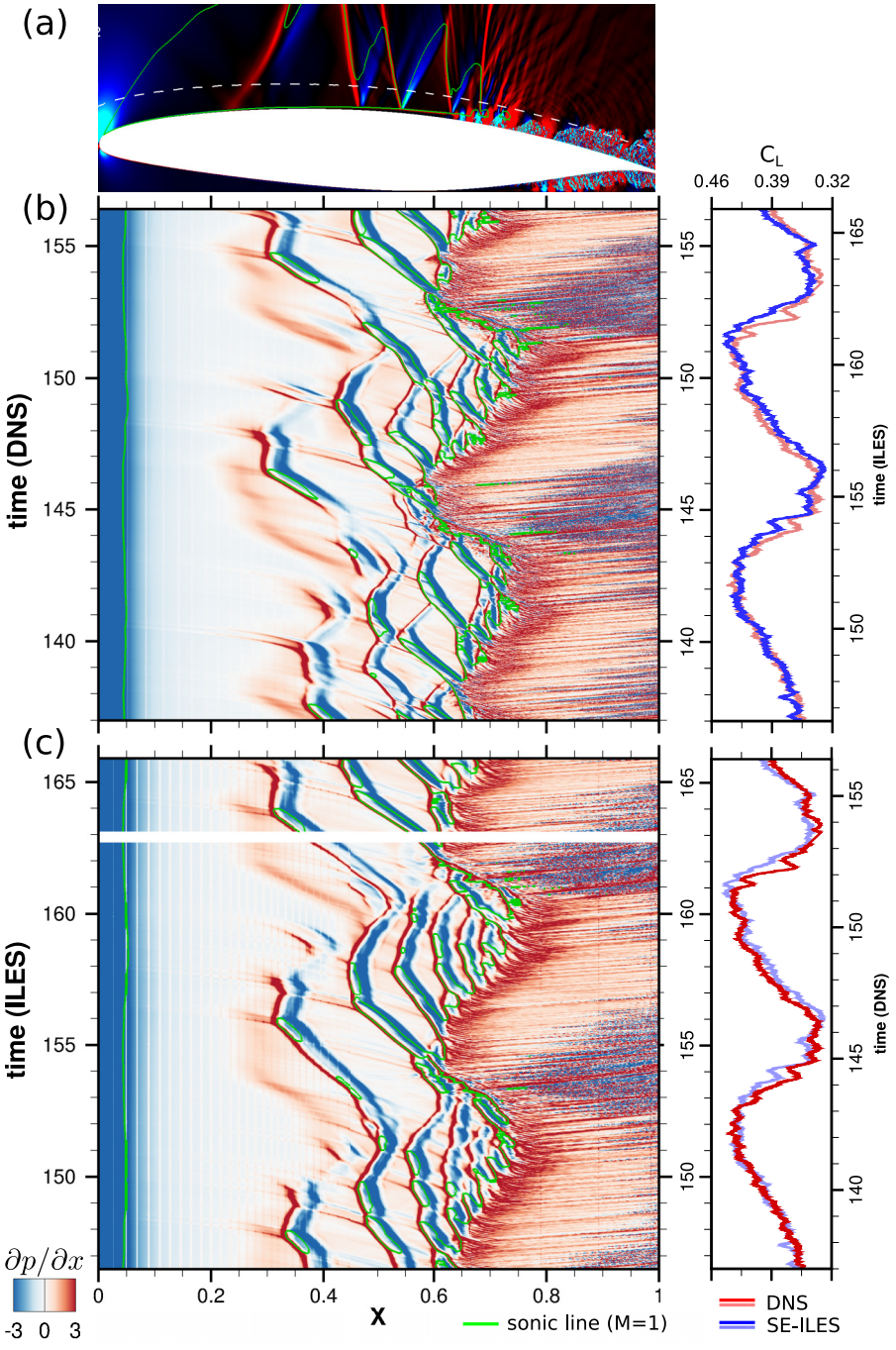

FIG. 3. (a) Snapshot showing contours of the streamwise pressure gradient of the DNS at $t = 156.4$. Contours of the streamwise pressure gradient of the narrow domain (b) DNS and (c) SE-ILES as a function of x and time along the white dashed curve in (a). Green curves denote the sonic lines and the lift coefficient is shown as a function of time for DNS (blue) and SE-ILES (red) on the right-hand side of the x/t diagrams. Please note that the time intervals are chosen to synchronize low-lift and high-lift phases of both simulations.

TABLE III. Overview of simulations discussed in Sec. IV.

Case	Name	α	Re	Grid points	L_z	N_z	Filter
$B0$	SE-ILES narrow	4°	500×10^3	75.3×10^6	$0.05c$	50	Targeted
$C0$	SE-ILES wide	4°	500×10^3	1.5×10^9	$1c$	1000	Targeted

lines initially correspond to the convection of Kelvin-Helmholtz roll-ups of the separated shear layer. Further downstream the lines are further apart and correspond to large-scale turbulent flow features, convecting over the airfoil surface. During low-lift phases, the large vortices appear as noisy patches near the trailing edge, showing up here because their influence reaches up to the white dashed monitor line in Fig. 3(a).

Further interesting details of the flow can be observed in Fig. 3(b). At $x \approx 0.05$, the green line indicates the beginning of the supersonic region. In the present case, shock trains are found in the region from $x = 0.3$ to $x = 0.6$ and usually consist of repeating patterns of a compression wave [red contours in Fig. 3(b)], followed by a subsonic region and an expansion fan [blue contours in Fig. 3(b)] turning the flow and returning it to a supersonic condition. The shock and expansion waves form a V-shaped structure in the xy plane, which is well pronounced around the half-chord location in Fig. 3(a). Where the compression waves meet the surface there is a thickening of the boundary layer due to the shock-wave/boundary-layer interaction, which can be observed in Fig. 3(a) at $x \approx 0.3$. On the other hand, in the same figure, acoustic waves generated downstream of the supersonic region propagate upstream, and slow down when approaching the supersonic region, where they strengthen and merge to form new shock waves.

All these flow features are remarkably consistent between the DNS version in Fig. 3(b) and the SE-ILES version in Fig. 3(c). None of the described phenomena are significantly different in the two figures, allowing us to have confidence that the SE-ILES are properly capturing the flow physics and can be used for further parametric studies. After having validated the SE-ILES method against a DNS, we will compare next the SE-ILES of this section with a simulation considering a much wider computational domain.

IV. EFFECT OF SPANWISE DOMAIN SIZE

In this section, we consider the impact of the spanwise domain extent on the buffet and related phenomena. It is of particular interest to confirm whether 2D phenomena, such as boundary-layer instabilities or shock waves reported by Ref. [37] (where studies were limited to $L_z \leqslant 0.25$), are preserved in much wider domains. We would like to be able to establish guidance for future DNS studies, by determining which phenomena can be safely studied in relatively narrow domains and which other phenomena, such as potentially highly three-dimensional separations, require much wider computational domains.

In this study, we use the same spectral-error-based large-eddy simulation (SE-ILES), which was validated in the previous section, and compare it to a corresponding simulation considering a 20 times wider domain ($L_z = 1c$). The details of the simulations are summarized in Table III as case $C0$.

An initial comparison of the effect of the massively increased computational domain is shown by the lift coefficient in Fig. 4. The solid black line shows the wide domain SE-ILES (case $C0$ in Table III) as a function of time, while the red line shows the narrow domain case ($B0$ from the previous section). To initialize the wide domain SE-ILES, a narrow domain SE-ILES solution was periodically replicated in the spanwise direction and left to evolve lower spanwise wave numbers. This transient phase of the wide domain SE-ILES is shown by the dashed gray line in figure 4. For case $C0$, representative time instances at high-lift and low-lift phases are labeled wide-domain

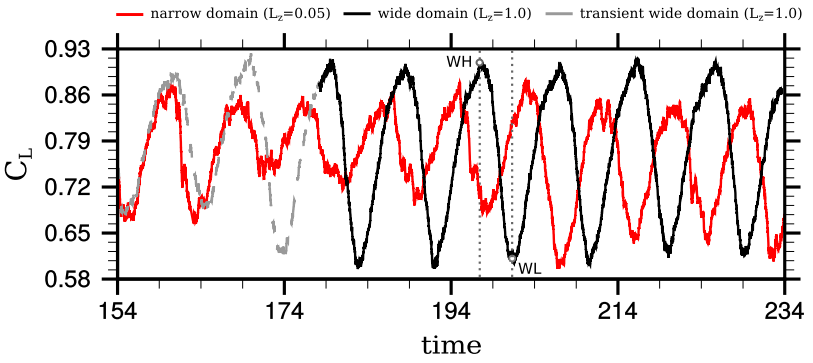

FIG. 4. Lift coefficient as a function of time for SE-ILES considering wide (black solid line) and narrow (red solid line) domains. The dashed gray line denotes the transient phase of the wide SE-ILES. Labels WH and WL correspond to snapshots in Fig. 11.

high-lift phase (WH) and wide-domain low-lift phase (WL), respectively, and will be discussed later with respect to Fig. 11.

Two observations can be made immediately from Fig. 4. First, the amplitude of lift oscillations increases significantly in the wider domain, and second, the oscillations become significantly more regular. As shown later in 3D visualizations of Sec. V B, the wide domain case exhibits larger vortical structures. The increased energy content captured by the wider domain seems to be the reason for increased amplitudes of lift oscillations. Despite the differences in unsteady lift coefficients, the mean values of aerodynamic coefficients summarized in Table IV agree well (±5%) for the wide and narrow domain cases. For example, the lift coefficient C_L only changes by 1% and the lift-to-drag ratio only changes by 3%. The drag coefficient C_D in Table IV is decomposed into skin-friction and pressure drag components according to $C_{D,f}$ and $C_{D,p}$, respectively. The contribution of the base pressure at the blunt trailing edge is denoted by $C_{D,p}|_{\mathrm{TE}}$ in Table IV. The mean trailing-edge pressure, which is often assumed to play an important role for buffet-related phenomena, does not seem to be affected by the domain size.

To analyze the variations observed in integral quantities in more detail, Fig. 5 shows time averages of the wall-pressure coefficient C_p [Fig. 5(a)] and skin-friction coefficient C_f [Fig. 5(b)] as a function of chord position x. The solid and dashed lines correspond to the suction side (SS) and pressure side (PS), respectively. The red line corresponds to the narrow domain, while the black line shows the wide domain. The dotted horizontal line in Fig. 5(a) indicates the critical pressure coefficient $C_{p,\mathrm{crit}}$ (i.e., the pressure coefficient, where an isentropic flow would reach sonic conditions) defined as

$$C_{p,\mathrm{crit}} = \frac{2}{\gamma M^2}\left[\left(\frac{2+(\gamma-1)M^2}{\gamma+1}\right)^{\frac{\gamma}{\gamma-1}} - 1\right], \tag{16}$$

corresponding under the present flow conditions to $C_{p,\mathrm{crit}} = -0.779$. The solid and dashed lines in Fig. 5(c) show the root mean square of the C_p and C_f fluctuations on the suction side, respectively.

TABLE IV. Aerodynamic coefficients. Values in parentheses denote the percental deviation from the wide domain case.

Name	C_L/C_D	C_L	C_D	$C_{D,f}$	$C_{D,p}$	$C_{D,p}\|_{\mathrm{TE}}$
SE-ILES wide	20.28 (±0%)	0.77 (±0%)	0.038 (±0%)	0.0038	0.034	−0.014
SE-ILES narrow	20.97 (+3%)	0.76 (−1%)	0.036 (−5%)	0.0037	0.032	−0.014

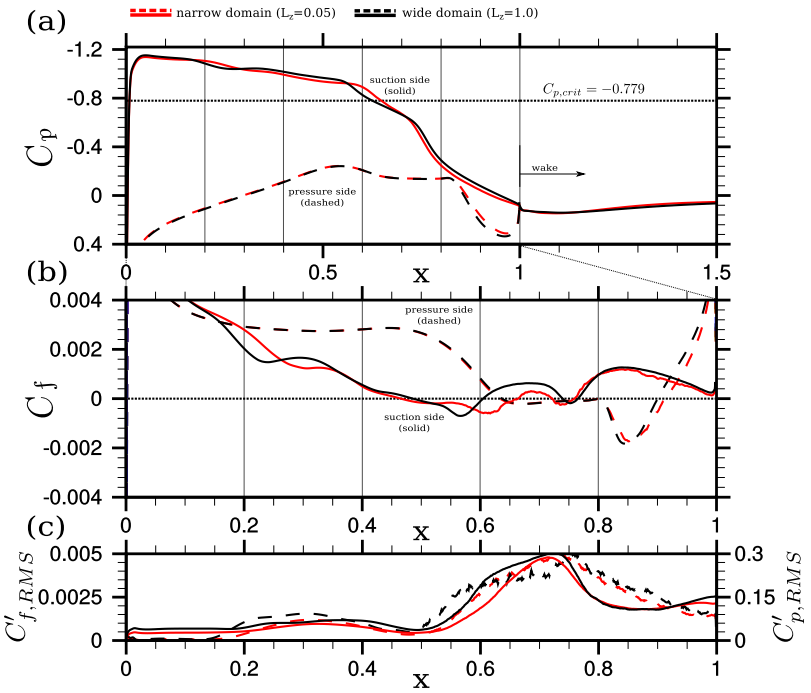

FIG. 5. Time- and span-averaged (a) pressure, (b) skin-friction coefficient, and (c) root mean square of corresponding fluctuations on the suction side as a function of chord position x for narrow (red) and wide domain (black) cases. Critical pressure coefficient $C_{p,\mathrm{crit}} = -0.779$ is indicated by the horizontal dotted line. In (a) and (b), solid and dashed lines correspond to suction and pressure sides, respectively, while solid and dashed lines in (c) denote $C'_{p,\mathrm{rms}}$ (right-hand-side scale) and $C'_{f,\mathrm{rms}}$ (left-hand-side scale), respectively.

A general observation again is that the mean flow is not very sensitive to the spanwise domain size. The pressure distribution is almost completely unchanged, while the skin friction shows a slightly (5%) earlier separation for the wide domain and the upper side C_f and $C'_{f,\mathrm{rms}}$, appear earlier and stronger in the wide domain case, consistent with the larger C_L variations.

In order to get a better impression of the unsteady flow features for both cases, we consider x/t diagrams for the narrow and wide domain cases, which are compared in Fig. 6. While the corresponding earlier Fig. 3(b) showed only a short time interval consisting of two low-frequency cycles, Fig. 6(a) shows contours of the streamwise pressure gradient for six buffet cycles. A corresponding x/t diagram is shown in Fig. 6(b) for the wide domain case. The general structure of the x/t diagrams has been already discussed in the previous section in connection with Fig. 3. Comparing the wide and narrow domain cases we see that the patterns are more regular in the wide domain case. In addition, we see a wider range of movement of the separation line in the wide domain case. Both observations are consistent with the changes seen in the lift time histories.

Given the greater regularity and repeatability of the wide domain simulation, it is worth exploring some of the features of the x/t diagrams in more detail. On the left-hand side of Fig. 6(b) at $x \approx 0.05$, the green line indicates the front end of the supersonic region, oscillating at a frequency similar to the lift coefficient, but slightly phase shifted. This oscillation is caused by varying the slope of the sonic line in the xy plane near the front of the airfoil and is not affected by the domain width. Above the laminar region in the range $0.2 < x < 0.5$, the path of shock waves is well approximated by the black dotted lines in Fig. 6(b) corresponding to a constant speed of $u_s = -0.09$. Considering the speed of sound in the free stream ($a = 1/0.7 \approx 1.43$), the Mach number of the upstream-propagating shock waves $M_s = -u_s/a \approx 0.06$ is significantly lower compared to acoustic

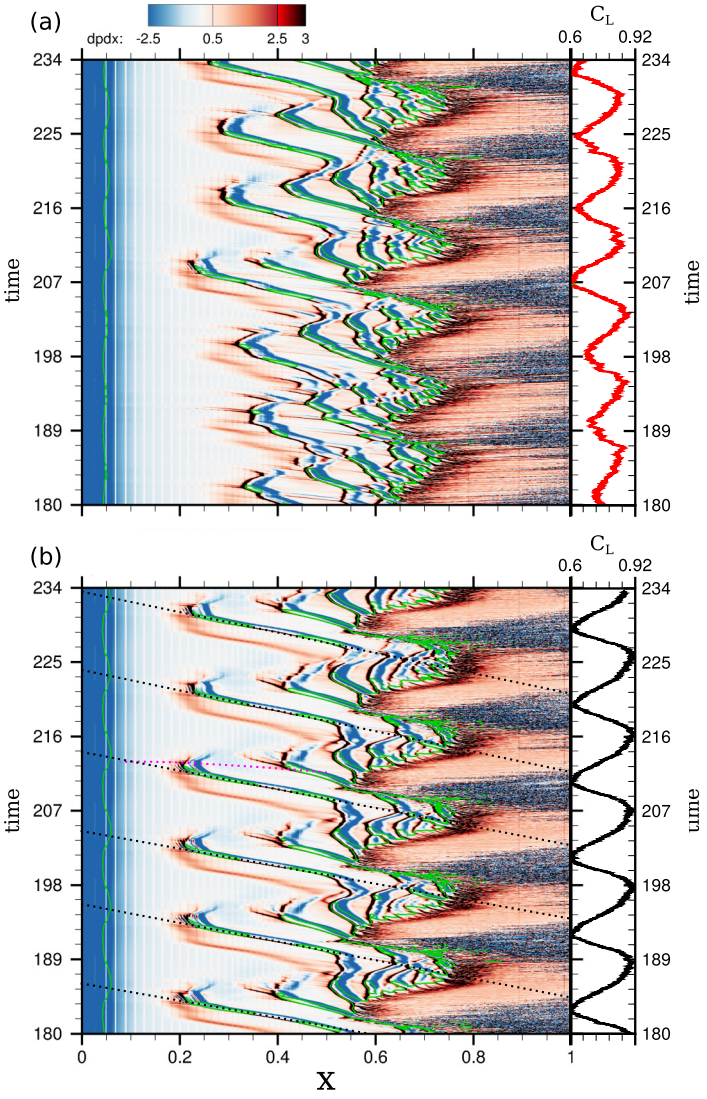

FIG. 6. Contour of the streamwise pressure gradient of the (a) narrow domain and (b) wide domain SE-ILES as a function of x and time at a distance of $\Delta y = 0.05c$ from the upper airfoil surface. Green curves denote the sonic lines and the lift coefficient is shown as a function of time for narrow (red) and wide domain SE-ILES (black) on the right-hand side of the x/t diagrams. Traces of shock waves and acoustic waves are indicated by black dotted and magenta dashed-dotted lines in (b), respectively. The lift coefficient is shown on the right-hand side of the contour plots as a function of time.

waves (sketched as a magenta dashed-dotted curve after 210 time units) propagating at $M_a \approx -0.14$. Also, neither the pressure ratio of $p_2/p_1 \approx 1.07$ nor the absolute level of the peak pressure in between the compression and expansion, i.e., $p_2 \approx 1.09$, vary significantly in that region. The green curves are interrupted just before half chord at $x \approx 0.4$, where the flow near the shock foot does not turn subsonic at the monitored location. Parallel to the shock waves, there are compression waves (so-called "separation shocks") moving ahead with the same speed and forming a lambda-shock structure with the mean shock, which is typical for laminar shock-wave/boundary-layer interactions

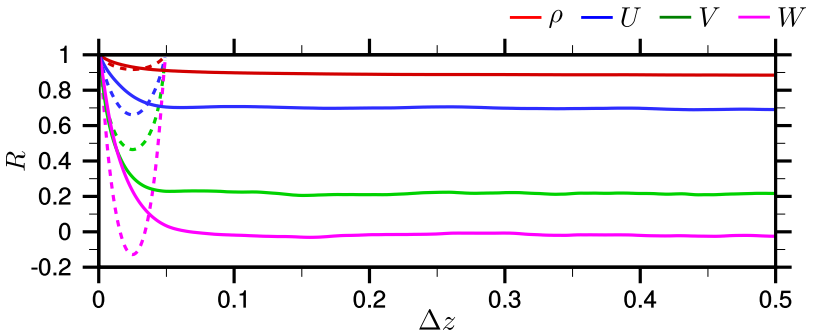

FIG. 7. Red, blue, green, and magenta lines show two-point correlations of density (ρ), streamwise- (U), vertical- (V), and spanwise-velocity (W) components, respectively. Solid and dashed lines correspond to the wide and narrow domain cases, respectively.

[13,57]. Both waves eventually disappear at $x \approx 0.2$, where the pressure ratio increases to $p_2/p_1 \approx 1.11$, and then vanish shortly after a brief downstream excursion. It is interesting to note that the continuations of the black dotted lines corresponding to the shock speed always intersect the front sonic line at their most downstream position, even though no shock features are observed in that region, suggesting that the upstream wave-propagation effects continue even when the shock themselves are no longer visible. Further discussions of the unsteady flow field will be provided in the next section, after we conclude the assessment of spanwise domain width effects.

A common method of assessing the suitability of the spanwise domain width is via two-point correlations, which in homogeneous directions should drop to zero over half the domain width. Here, we consider a fixed position close to the suction-side trailing edge with a wall-normal distance of $\Delta y \approx 0.06$ ($x = 1.0035$ and $y = -0.0015$). The averaged two-point correlation R is calculated according to

$$R_{(\Delta k)} = \frac{1}{N_z N_t} \sum_{k=1}^{N_z} \sum_{t=1}^{N_t} \frac{q'_{(k,t)} q'_{(k+\Delta k,t)}}{|q'_{(k,t)}||q'_{(k+\Delta k,t)}|} \quad \text{for} \quad \Delta k \in [0, N_z], \quad t \in [0, N_t], \tag{17}$$

$$\Delta z = \frac{L_z}{N_z} \Delta k, \tag{18}$$

where the vector $q'_{(k,:)}$ contains a time series of the fluctuations in the quantity of interest at a fixed position in the xy plane at the kth point in the spanwise direction, which is projected onto vector $q'_{(k+\Delta k,:)}$ and normalized by the magnitudes of both vectors. Finally, the average value is calculated for each Δk, looping through each point in the spanwise direction ($1 < k < N_k/2$), and transformed to the physical distance Δz, using Eq. (18). Figure 7 shows the two-point correlations for both cases (solid lines for the wide domain and dashed lines for the narrow domain), where the red, blue, green, and magenta lines correspond to density (ρ), streamwise- (U), vertical- (V), and spanwise-velocity (W) components, respectively. The extreme cases for the wide domain are the density, which remains highly correlated ($R = 0.9$), and the spanwise velocity, which drops to $R = 0$ for $\Delta z > 0.075$. What we are seeing in the two-point correlations is the effect of two distinct phenomena in the flow field. The periodic motion associated with buffet (as shown in the next section) is essentially two dimensional, hence the density field remains highly correlated across the span. However, the superimposed turbulence is three dimensional and contained within the domain, so that the spanwise velocity correlations drop to zero within $\Delta z = 0.075$. The spanwise velocity is different to the other velocity components since it has a spanwise-mean value that is constant (equal to zero) during all phases of the buffet cycle.

In the narrow domain (shown with the dashed lines in Fig. 7 for the full range of possible Δz) the spanwise two-point correlations do not decay to zero even for the spanwise velocity component.

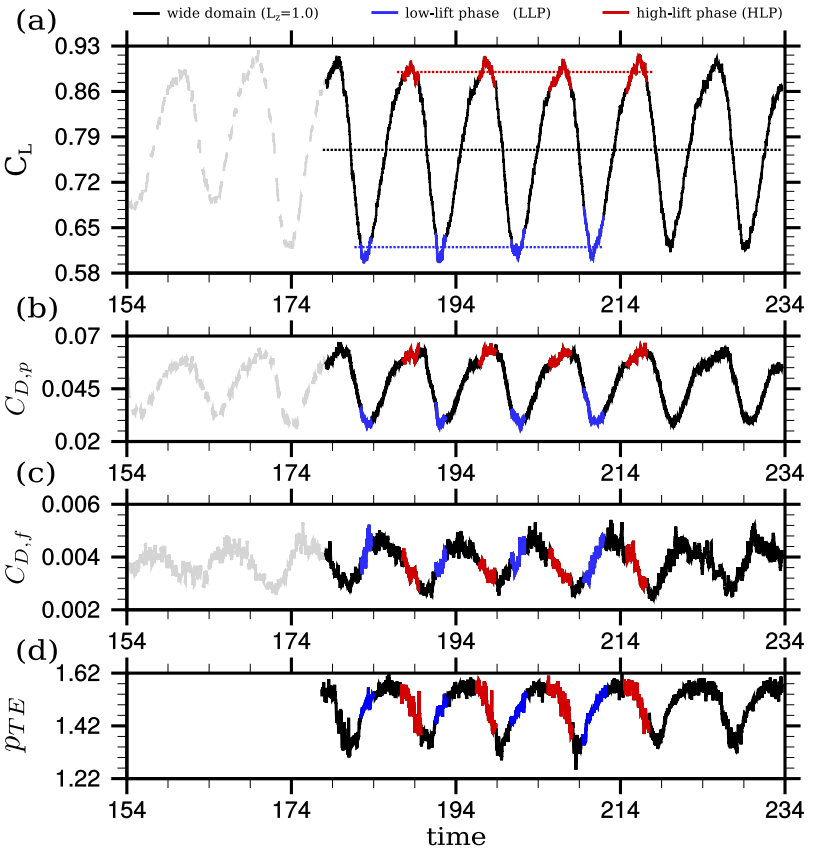

FIG. 8. Extraction of high-lift and low-lift statistics: (a) Variation of lift coefficient with time, showing in red the high-lift samples and in blue the low-lift samples, (b) pressure-drag coefficient, (c) skin-friction drag coefficient, and (d) trailing-edge pressure.

Despite this, and in common with the experience of other flows in restricted (but not minimal) domains [58], the flow phenomena are representative of the wider domain case, so that such narrow domain simulations can still be useful.

V. FURTHER ANALYSIS OF THE WIDE DOMAIN CASE

In this section we look in detail at statistics and instantaneous flow fields from representative phases of the buffet cycle, exploiting the large amounts of data available for the wide domain case. To begin with, we focus in Sec. V A on phase-averaged data collected during high- and low-lift phases (denoted by HLP and LLP, respectively). In Sec. V B we analyze instantaneous 3D visualizations at representative time instances during high- and low-lift phases, which allow us to study the spanwise characteristics of transition, shock waves, and low-frequency phenomena. Finally, in Sec. V C, we consider the global behavior of low-frequency phenomena associated with transonic buffet, including the flow over the pressure side of the airfoil.

A. Phase-averaged flow fields

The regularity of the buffet cycle in the wide domain case allows us to extract reliable phase-averaged statistics. Figure 8(a) shows in red and blue the sections of the lift history that were used

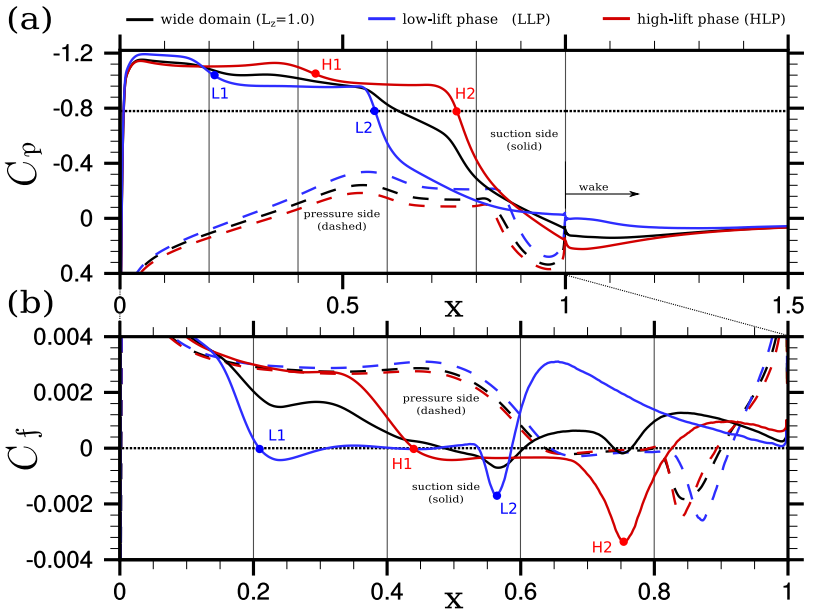

FIG. 9. Extraction of high-lift (red) and low-lift (blue) statistics corresponding to Fig. 8: (a) Pressure coefficient, including the critical value denoted by the dashed-dotted black line, and (b) skin-friction coefficient. The upper surface is shown with solid lines and the lower surface with dashed lines.

to create averages over the high- and low-lift phases of the buffet cycle. Figures 8(b) and 8(c) show respectively the pressure drag and skin-friction drag coefficient, with the trailing-edge pressure measured at the upper-side corner in Fig. 8(d). The pressure drag is broadly in phase with the lift coefficient, although the pressure drag has a slightly delayed peak and has a sharper drop during the decreasing-lift part of the cycle. Skin-friction and trailing-edge pressure are roughly in phase with each other (the trailing-edge pressure lags slightly), and both lead the lift by about a quarter of a cycle. The friction drag, for example, reaches a minimum when the transition takes place at its most downstream position ($x > 0.7$), just before the lift reaches its minimum.

Figure 9 shows in red and blue wall-pressure [Fig. 9(a)] and skin-friction coefficient [Fig. 9(b)] as a function of x corresponding to high- and low-lift phases in Fig. 8(a). Figure 9(a) is continued into the near wake to show the pressure variations downstream of the trailing edge. Key features are identified on the figure. Points H1 and L1 correspond to the first occurrences of flow separation ($C_f = 0$) on the upper surface (denoted with the solid lines). The initial separation is significantly earlier in the low-lift phase, after which there is an extended region with C_f close to zero. Although the separation is later in the high-lift phase, there is still an extended region of reverse flow present. Points H2 and L2 correspond to the crossing of the critical pressure, i.e., the isentropic sonic condition, and it is notable that in both cases these points correspond to the minimum skin friction from Fig. 9(b), i.e., with the location of the peak strength of the reverse-flow vortex that precedes reattachment. The pressure gradient at H2 and L2 and the upstream-pressure plateau hardly change during the low-frequency cycles, while the blue curve flattens at $x > 0.6$ converging to a higher trailing-edge pressure. Considering the Rankine-Hugniot equations modeling the pressure jump across a shock wave, the shock strength is solely defined by the pressure and relative Mach number of the shock wave. This would suggest that shock waves terminating the supersonic region at high- and low-lift phases have the same strength on average. It is also interesting to note that, superficially, the C_p curves in Fig. 9(a) resemble the picture we would expect for a single shock wave oscillating back and forth over $0.5 < x < 0.8$. Strong gradients are removed by time averaging,

TABLE V. Aerodynamic coefficients. *Values in parentheses denote the percental deviation from the total.

Name	C_L/C_D	C_L	C_D	$C_{D,f}$	$C_{D,p}$	$C_{D,p}\|_{\mathrm{TE}}$
HLP	17.91 (−12%)	0.89 (+16%)	0.049 (+29%)	0.0036	0.046	−0.014
Total*	20.28 (±0%)	0.77 (±0%)	0.038 (±0%)	0.0038	0.034	−0.014
LLP	29.24 (+44%)	0.62 (−19%)	0.021 (−45%)	0.0039	0.017	−0.013

so that the black curve is reminiscent of the full-time statistics of experiments at high Reynolds numbers [31]. However, the instantaneous flow field looks quite different, as we observe multiple upstream-propagating shock waves in Fig. 6(b) and animations. The animation [59] shows contours of the axial pressure gradient similar to Fig. 3(a). Due to the decreased resolution above the fore part of the airfoil ($x < 0.2$), grid-to-grid point oscillations can occasionally be seen as multiple stripes parallel to oblique shock waves in the visualizations, e.g., at $t = 184$. These grid-to-grid point oscillations are exaggerated by the narrow color-map scaling ($-5 < \partial p/\partial x < 5$) and show no impact on the boundary layer.

Table V summarizes the aerodynamic coefficients from these two flow phases and gives their relative departure from the time average, which is up to 19% in the case of the lift coefficient and 45% for the drag coefficient. However, it is also interesting that some quantities, such as the friction contribution to drag and the base-drag coefficient $C_{D,p}|_{\mathrm{TE}}$ (integrating pressure contributions along the blunt trailing edge), vary by less than 10%.

To link more clearly the boundary-layer behavior with the external flow field, Fig. 10 shows span-averaged contours of the long-time-averaged Mach number, comparing the corresponding sonic line in black with the same line in the high- and low-lift phases shown by the red and blue lines, respectively. Figure 10(a) shows the whole supersonic region, while Fig. 10(b) focuses on the boundary layer. Both parts of the figure are distorted by stretching the y coordinate, more severely

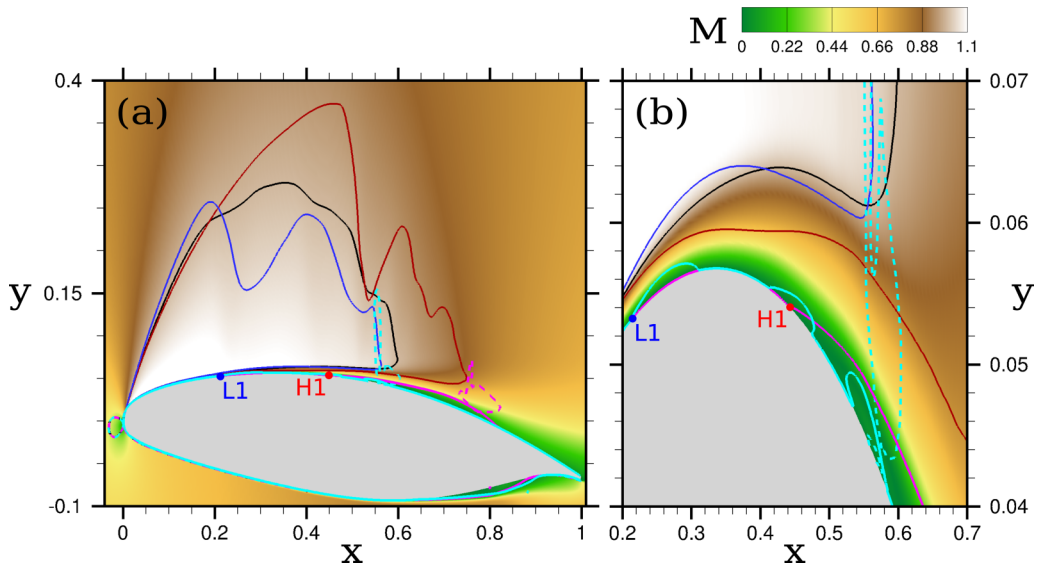

FIG. 10. Contours showing the time- and span-averaged Mach number of case $C0$. Solid black, red, and blue curves denote sonic lines corresponding to full time-averaged, high-lift, and low-lift phase-averaged flow fields, respectively. Dashed light-blue and magenta lines indicate a high adverse pressure gradient for the low-lift phase (LLP) and high-lift phase (HLP), respectively. Magenta and light-blue solid lines denote isocurves of streamwise velocity $u = 0$. Both (a) and (b) are distorted.

in Fig. 10(b). As well as the sonic line, the figures show the $u = 0$ contour (in magenta and light blue for low- and high-lift phases, respectively) and dashed lines show the region of the strongest adverse streamwise pressure gradient. While the region of flow reversal on the pressure side hardly changes between the high- and low-lift phases, we can observe the significantly larger region of flow reversal consistent with the skin-friction plots in Fig. 9(c). The supersonic region is clearly larger in the high-lift phase, with oscillations in the sonic line after the half chord showing the time-averaged effect of the shock/expansion combination, while such oscillations extend throughout the supersonic region in the low-lift phase. As seen in the x/t diagrams there are more than one of these shock/expansion waves, in contrast to the standard picture of buffet involving a single shock oscillating back and forth. The region of highest-pressure gradient (the dashed lines) can be interpreted at the averaged effect of the multiple propagating shock waves seen in the present configuration and is, again, more consistent with the standard picture of where a shock would occur: further upstream during the low-lift phases and further downstream during the high-lift phase. In addition to longitudinal regions oriented orthogonal to streamlines, which are reminiscent of shock waves, we also observe regions near the wall showing high-pressure gradients. These regions seem to be caused by upstream-propagating acoustic waves accumulating near the sonic line. These regions are larger during high-lift phases and may be the reason for the increased pressure gradient at the rear part of the airfoil [observed in Fig. 9(b)].

B. Instantaneous 3D visualizations

More information, particularly relating to the transition process, can be gained from visualizations of the flow fields at high- and low-lift instants. These were identified in Fig. 4 as time instants WH and WL, respectively, for the wide domain case. A common practice to visualize vortex structures is the so-called Q criterion, defining vortices as a local imbalance of vorticity and shear strain according to

$$Q = \tfrac{1}{2}(||\Omega||^2 - ||S||^2) = \tfrac{1}{2}(u_{ii}u_{jj} - u_{ij}u_{ji}), \tag{19}$$

where Ω denotes the vorticity tensor and S the strain-rate tensor. Figure 11 shows a combination of side (x-y) and top views (x-z) using an isosurface of $Q = 100$ colored by the magnitude of the velocity, which serves to identify the key flow features for further discussion. The Q-criteria surfaces are only plotted for the upper part of the wake to help distinguish coherent vortical structures. In addition, the side view shows contours of the streamwise pressure gradient and the white line is the instantaneous sonic line. At the high-lift condition the separation point is further aft and we have a much narrower wake compared to the low-lift condition. Associated with this we have a large supersonic region, extending beyond the half-chord location in the high-lift condition, whereas in the low-lift condition we have a series of shocks and expansions over the front part of the airfoil, reminiscent of the shock train of Ref. [60].

In the top views of Fig. 11 we can observe the transition process and get an impression of the size of turbulent structures in the separated flow region and extending into the wake. In the low-lift phase we see clear evidence for Kelvin-Helmholtz roll-ups (i.e., arising from an inflectional instability) of the separated shear layer, with about six successive roll-ups visible for $x < 0.5$. Similar structures were observed over a high-pressure turbine vane cascade at a comparable Reynolds number and predicted by linear stability methods in boundary layers near flow separation (velocity profiles exhibit deflection points) [61]. The presence of Kelvin-Helmholtz roll-ups does not exclude a possible connection to Tollmien-Schlichting waves in the upstream boundary layer, though the significant amplification seen here is associated with the strong inflectional instability.

These Q structures are continuous across the span, with a slight waviness, which may be caused by linear instabilities with large spanwise wave numbers [61]. The first spanwise dislocations are visible at the midchord location $x = 0.5$, followed by a rapid breakdown to turbulence, attributed in previous work [37] to a three-dimensional self-sustained instability of the unsteady large-scale

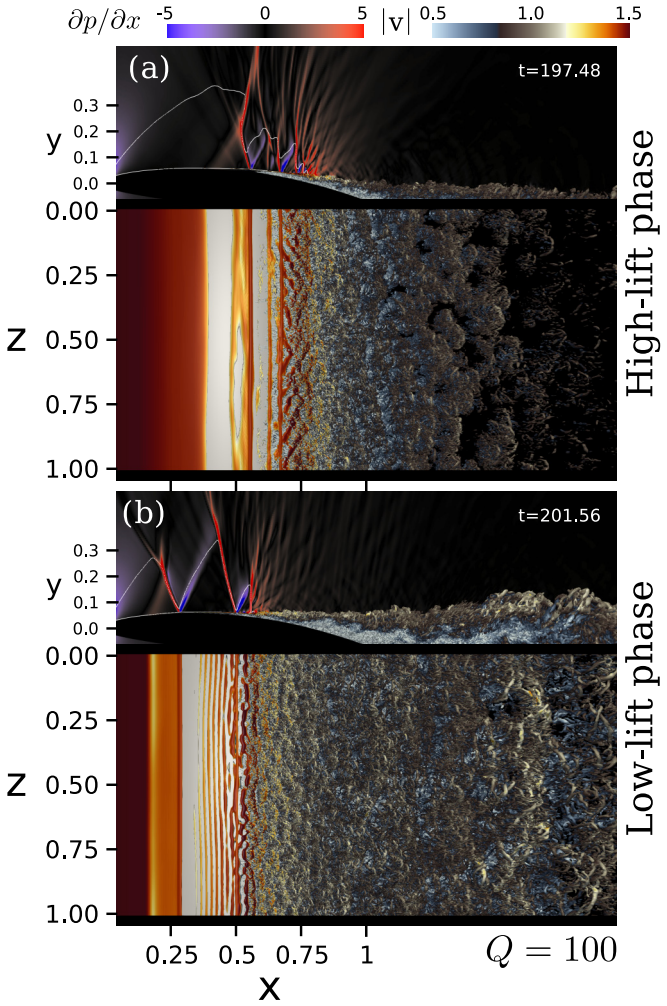

FIG. 11. Instantaneous 2D slices [side view (x-y) and top-down view (x-z)] showing Q-criterion surfaces ($Q = 100$) colored by velocity magnitude at the (a) high-lift and (b) low-lift phase corresponding to labels WH and WL in Fig. 4, respectively.

structures. In the developing flow downstream of the transition we observe the formation of larger-scale structures, but these are still comfortably contained within the large computational domain.

Additional features of the flow upstream of transition are Q structures that form as the flow is turned at the edge of the boundary layer due to shock/expansion combinations that cause a local thickening and then thinning of the boundary layer. Examples are seen at $x \approx 0.28$ in the high-lift phase and $x = 0.55$ in the low-lift phase in Fig. 11(a). We have observed similar structures in shock-induced separation bubbles, where the flow at the apex of the bubble turns rapidly in response to the impinging shock wave, also resulting in a reflected expansion wave. The interesting feature here is that these structures show almost no variation across the span, even in the wide domain, despite the turbulent flow regions being fully three dimensional.

In the high-lift phase, seen in Fig. 11(a), transition appears to follow directly from the Q structures that form from the shock-wave/boundary-layer interaction [62]. The spanwise structure at $x = 0.66$ is followed by a cross-hatched pattern of structures corresponding to a spanwise wavelength of $\lambda_z \approx 0.07$ and suggesting an oblique mode of instability preceding the final breakdown

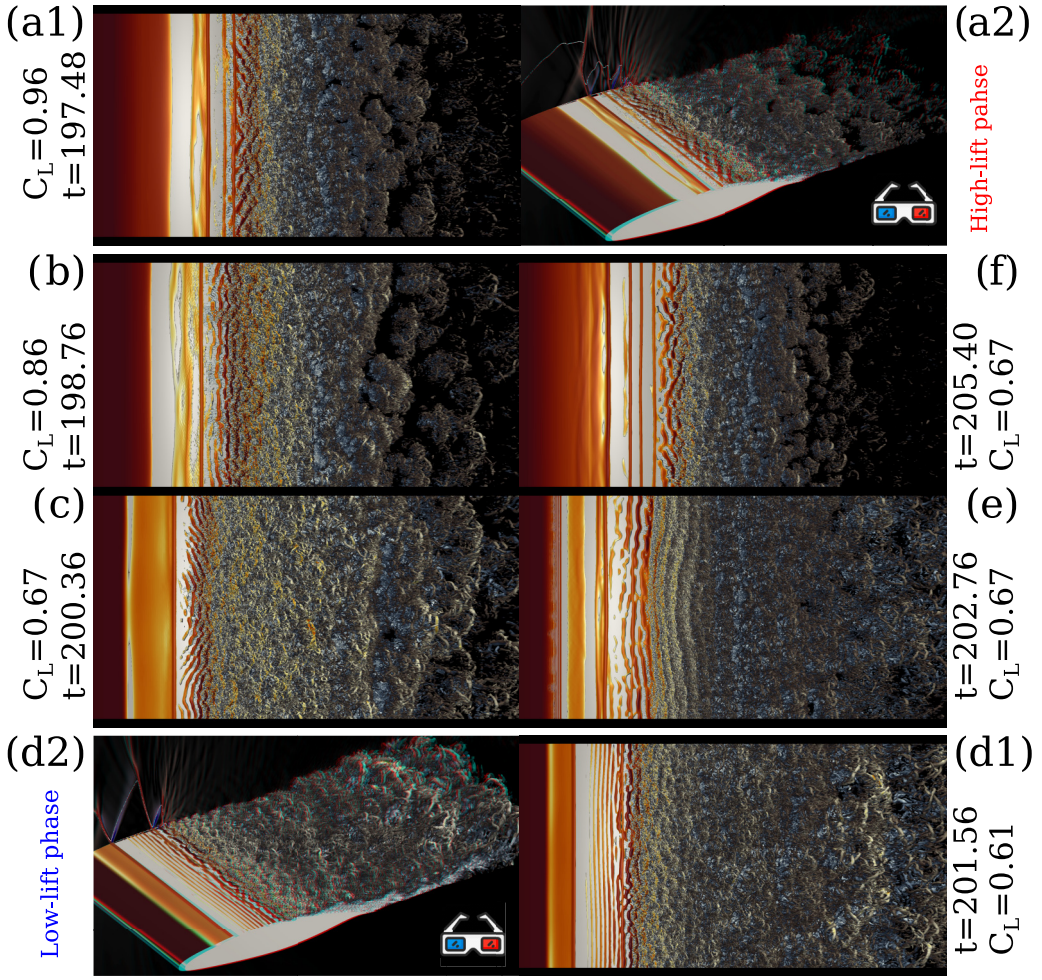

FIG. 12. Top-down view (x-z) showing Q-criterion surfaces ($Q = 100$) colored by velocity magnitude. Perspective (stereo 3D) views at (a2) HLP and (d2) LLP.

to turbulence [63,64]. The transition process continues up to $x = 0.8$ in this case, after which larger-scale turbulent features emerge. The wake is more intermittent in the high-lift phase and shows large-scale structures roughly up to a fifth of the domain width.

Figure 12 shows the variation of the Q structures during the complete buffet cycle, considering four intermediate phases [in Figs. 12(b), 12(c) 12(e), and 12(f)] in between the high-lift phase in Fig. 12(a) and the low-lift phase in Fig. 12(d). The high- and low-lift phases are also shown respectively in perspective (stereo 3D) views in the top right and bottom left of the figure, which show more clearly the large-scale structures in the near-wake region. The main features of the other plots have already been described in connection with Fig. 11. Considering the whole buffet cycle in Fig. 12, we see the forward and backward movement of the separation location and the strict two-dimensionality of the shock-train patterns. The only indication of potentially larger-scale structures is the spanwise waviness of the transitional flow structures seen in Fig. 12(e), but these are a weak feature and are only present for a small part of the buffet cycle. Similar to the present study, no significant 3D structures were observed in experiments by Ref. [65] on a two-dimensional NASA common research model (CRM) airfoil, however, stall and buffet cells have been reported

by Refs. [66,67] at spanwise wavelengths $\lambda_z > 1c$ for different airfoil geometries. One would have expected to see significant larger-scale features already in the present wide domain simulation in the case that stall/buffet-cell behavior was relevant for this airfoil at this flow condition, although it is not possible to say for sure that they would not form in even wider computational domains.

C. Global behavior of low-frequency phenomena

Having confirmed that the low-frequency phenomenon associated with buffet has a significant 2D component, we next consider additional x/t diagrams at $z = 0$. While we focused in Fig. 6 on the behavior of shock waves and acoustic waves, we now consider the overall characteristics of the flow undergoing buffet. Contours in Fig. 13 show fluctuations of isentropic Mach number fluctuations at the airfoil surface [Fig. 13(a)] and Mach number fluctuations along a monitor line outside the boundary layer [Fig. 13(b)] (at $\Delta y = 0.05$ from the surface). The left part of both plots in Fig. 13 shows the pressure sides, while the right part shows the suction sides (the sketches on the top indicate active monitor curves by solid lines and inactive ones by dotted curves). The x axis of the pressure-side plots has been reversed so that the trailing edge corresponds to the extreme left and right edges of the figure, while the leading edge is located at the center. The isentropic Mach number is commonly used to estimate locations of shock waves in experiments, using only the wall pressure [68] and is computed here according to

$$M_{\mathrm{is}} = \sqrt{\left[\left(\frac{p_0}{p}\right)^{\frac{\gamma-1}{\gamma}} - 1\right]\frac{2}{\gamma-1}}. \tag{20}$$

Fluctuations of Mach numbers in Fig. 13 are defined as

$$M' = \frac{M - \overline{M}}{\overline{M}}, \tag{21}$$

where $\overline{M}$ denotes the local time average. While Fig. 6 focused our attention on shock waves and acoustic phenomena associated with intermediate and small timescales (St > 0.4), Fig. 13 highlights low-frequency phenomena corresponding to St < 0.4.

Considering first Fig. 13(a) at the airfoil surface, we observe at the right of the figure a periodic pattern moving downstream with a speed of $v_c \approx 0.098$, representing a slow adjustment of the reattached boundary layer. After encountering the trailing edge, this pattern then continues propagating along the pressure side, but in the upstream direction at a velocity of $v_u = -0.364$ [deduced from the positive slope on the left plot in Fig. 13(a)]. At the leading edge, we observe a phase shift between the suction and pressure side, which means that the flow is accelerating on one side, while it is decelerating on the other side. On the upper side we can observe weak indications of downstream-moving structures in the Mach contours near the leading edge [positive slope on the right-hand plot in Fig. 13(a) corresponding to a velocity of $v_c \approx 0.113$ at $x \approx 0.2$]. For $x > 0.2$, these structures then disappear or are hidden by upstream-propagating structures with a negative slope on the right-hand plot in Fig. 13(a) in the range of $0.2 < x < 0.6$. Near the transition region we observe a patchy green sonic line undergoing the low-frequency oscillations associated with transonic buffet. This is reminiscent of the traditional picture of transonic buffet, where only a single shock wave is moving back and forth [27,69].

The shock waves are clearer in Fig. 13(b), showing fluctuations of the Mach number along a monitor line $\Delta y = 0.05$ away from the surface. The green sonic lines correspond to those shown previously in Fig. 6(b). The upstream-propagating shock waves seem to move only during phases where Mach numbers are lower than the time average corresponding to blue corridors, in good agreement with the discussion of Fig. 13(a). While we observe multiple shock waves per low-frequency cycle at $x \approx 0.5$, we observe only one shock wave per cycle at positions further upstream ($x < 0.3$). A striking qualitative difference between the two monitor curves shown in Figs. 13(a) and 13(b) is observed near the suction-side trailing edge, where the structures within and outside

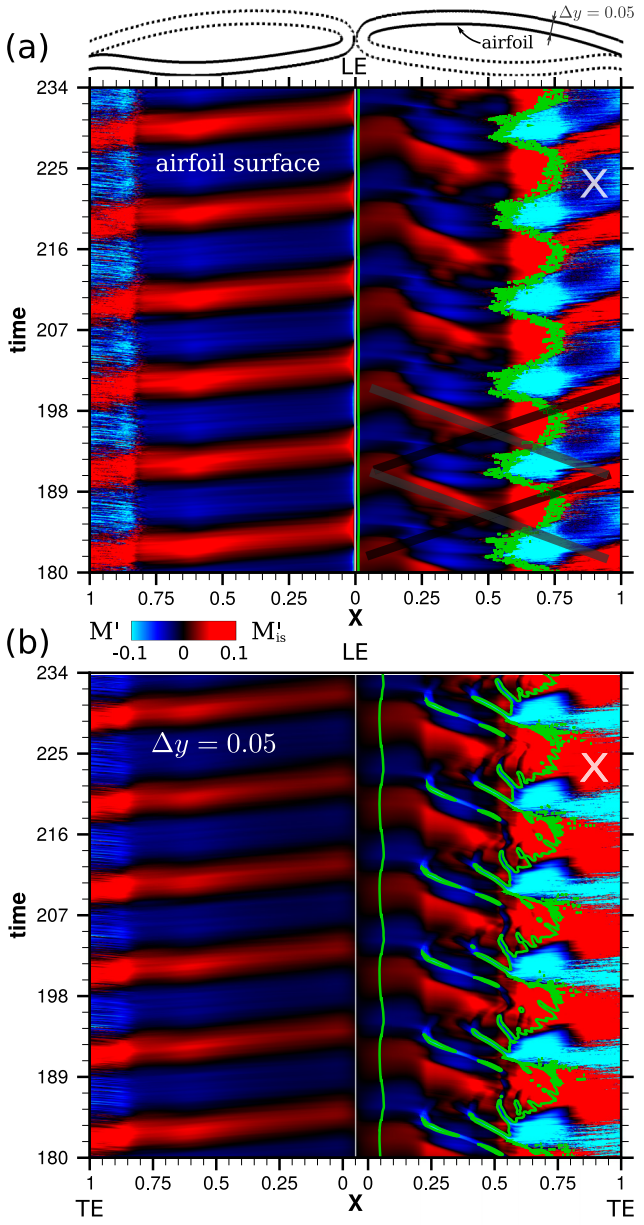

FIG. 13. Contours showing (a) isentropic Mach number fluctuations at the airfoil surface and (b) Mach number fluctuations along an isocurve outside the boundary layer as a function of space and time, respectively. The green lines denote sonic lines.

the boundary layer are completely different, as, for example, highlighted at $t \approx 225$ by the white cross. The underlying wave structure is revealed in the isentropic Mach number fluctuations, but obscured in the Mach number plot. The remaining features of Fig. 13(b) agree well with Fig. 13(a) or have been already discussed in connection with the pressure-gradient field in Fig. 6(b).

Lines have been added to the first two low-frequency cycles of the upper side plot in Fig. 13(a), to illustrate the form of a standing-wave pattern between the suction-side leading edge and trailing

edge, as previously seen in Ref. [37]. The role of the trailing edge in the buffet cycle has been the subject of some previous experiments, for example, by adding splitter plates to the trailing edge [70]. Even though buffet could be suppressed in some cases, there were also cases showing no effect or just a change in the buffet characteristics. This suggests that the behavior on the pressure side can affect the low-frequency phenomenon, but is not necessarily part of the mechanism that drives the buffet. The work of Ref. [71] supports this assumption, as they applied selective frequency filtering on the pressure side without affecting the buffet phenomenon significantly. This would mean that, also in our case, the pressure side is only reacting to changes in the flow field induced by the suction side via the trailing edge.

A question arising from the present work is the significance of the leading-edge phase shift. This could just be a random shift, due to the different arrival times of waves from the lower and upper sides, or it could be that the weak downstream-propagating wave, observed on the suction side near the leading edge, plays a role in connecting the pressure side disturbances to the boundary layer on the suction side, upstream of its separation point. This aspect deserves further study.

VI. CONCLUSIONS

A comparison has been made of transonic buffet, captured in simulation with widely different spanwise domain sizes and span-periodic conditions. The configuration is based on an unswept laminar-flow supercritical airfoil (Dassault Aviation's V2C profile) at a free-stream Mach number of 0.7 and Reynolds number of 500 000. The numerical approach was based on a large-eddy simulation, using a spectral estimate to control the level of local filtering applied. Initially, a narrow domain simulation was used to validate the numerical approach against a direct numerical simulation. Then an LES was run in a domain 20 times wider, with the same x-y grid and 20 times the number of points in the spanwise direction.

It was found that the narrow domain was sufficient to capture the flow physics of the buffet cycle, with the lift-to-drag ratio, for example, being within 3%. In terms of the usual measures used to assess the effect of domain width, it was found that two-point correlations mostly failed to fall to zero. This is due to the continued two-dimensionality of the potential flow outside the boundary layer, including the pattern of upstream-propagating shock waves. The exception was the spanwise velocity which, since it only depends on the turbulent flow, fell to zero within a spanwise separation an order of magnitude smaller than the domain width.

Quantitative effects of the increasing domain width included the increasing regularity of the buffet cycle and the increased amplitude. These effects were both attributed to the increased capture of large-scale structures near the trailing edge. The increased energy of these can lead to high buffet amplitudes and the larger statistical sample of such structures in the wide domain can lead to greater regularity, since the conversion to two-dimensional waves at the trailing edge is averaged over more structures.

The transition mechanism was studied at representative instants of high- and low-lift phases of the buffet cycle. At low lift the transition proceeded via Kelvin-Helmholtz structures and a rapid breakdown consistent of a kind seen before. At the high-lift condition the transition proceeds from span-uniform structures imposed by upstream-propagating shock waves reflecting as expansion waves. Such structures show up clearly in Q isosurfaces, with the transition following via oblique modes rather than via two-dimensional Kelvin-Helmholtz waves. There was no sign of stall cells, with the only large-scale three-dimensionality being a slight waviness in the Kelvin-Helmholtz structures.

Phase-averaged statistics from the wide domain simulation provide an impression of a single back and forth moving shock wave, while instantaneous data show multiple upstream-propagating shock waves. Considering the global flow field, the pressure side was found to be linked with the unsteady flow over the suction side via upstream propagation of acoustic waves originating at the trailing edge that can be traced back to the separation region by a slow downstream propagation that is visible in isentropic Mach number contours. Upstream-propagating waves also appear over the

suction side where they may connect to the pressure side waves near the leading edge, the precise role of which needs further study.

The source code to compile the SE-ILES grid (it was not possible to include Dassault Aviation's V2C profile), a PYTHON code for two-point correlation, data corresponding to Figs. 2–6, 8, 9, and 13, and animations are openly available from the University of Southampton repository [72]. Animations are also accessible via YouTube [73].

The corresponding data set also contains additional quantities along monitor lines at the airfoil surface and outside the boundary layer as a function of chord position and time, which were not discussed in this work, but may be of interest of the research community.

ACKNOWLEDGMENTS

We are grateful for computational resources provided by the Partnership for Advanced Computing in Europe (PRACE grant entitled "TRAAD - TRansonic Airfoil AeroDynamics") on the HazelHen supercomputer (HLRS), by the Engineering and Physical Sciences Research Council (EPSRC), ARCHER (Leadership grant entitled "Transonic flow over an aerofoil"), and UKTC (EPSRC Grant No. EP/L000261/1) on the U.K. national supercomputer ARCHER, and by the University of Southampton on the Iridis clusters. M.Z. was supported by an EPSRC studentship award (Reference No. 1665277) and by an EPSRC grant entitled "Extending the buffet envelope: step change in data quantity and quality of analysis" (EP/R037027/1).

[1] D. G. Mabey, A review of scale effects in unsteady aerodynamics, Prog. Aerosp. Sci. **28**, 273 (1991).

[2] E. Stanewsky and D. Basler, Experimental investigation of buffet onset and penetration on a supercritical airfoil at transonic speeds, in *Proceedings of Aircraft Dynamic Loads Due to Flow Separation*, AGARD Conference Proceedings No. 483 (AGARD, London, 1990), pp. 4:1–11.

[3] B. H. K. Lee, H. Murty, and H. Jiang, Role of Kutta waves on oscillatory shock motion on an airfoil, AIAA J. **32**, 789 (1994).

[4] N. F. Giannelis, G. A. Vio, and O. Levinski, A review of recent developments in the understanding of transonic shock buffet, Prog. Aerosp. Sci. **92**, 39 (2017).

[5] H. Tijdeman, *On the motion of shock waves on an airfoil with oscillating flap, in Symposium Transsonicum II, International Union of Theoretical and Applied Mechanics Series* (Springer, Berlin, 1975), pp. 49–56.

[6] M. T. Landahl, Some developments in unsteady transonic flow research, in *Symposium Transsonicum II* (Ref. [5]), pp. 1–32.

[7] S. Raghunathan, M. Gillan, R. Cooper, R. Mitchell, and J. Cole, Shock oscillations on biconvex aerofoils, Aerosp. Sci. Technol. **3**, 1 (1999).

[8] B. Lee, Self-sustained shock oscillations on airfoils at transonic speeds, Prog. Aerosp. Sci. **37**, 147 (2001).

[9] C. Tulita, E. Benard, and S. Raghunathan, Transonic periodic flow subject to adaptive bump, in *41st Aerospace Sciences Meeting and Exhibit*, January (American Institute of Aeronautics and Astronautics, Reston, VA, 2003), pp. 1–15.

[10] F. Tamaki, Experimental studies on the stability of the transonic flow past airfoils, J. Phys. Soc. Jpn. **12**, 544 (1957).

[11] L. Trilling, Oscillating shock boundary-layer interaction, J. Aerosp. Sci. **25**, 301 (1958).

[12] R. J. Hakkinen, I. Greber, L. Trilling, and S. Abarbanel, *The Interaction of an Oblique Shock Wave with a Laminar Boundary Layer*, Tech. Rep. NASA-Memorandum-2-18-59W (Massachusetts Institute of Technology, Cambridge, MA, 1959).

[13] K. Karashima, Instability of Shock Wave on Thin Airfoil in High Subsonic Flow, Tech. Rep. Report No. 363
(Aeronautical Research Institute, University of Tokyo, 1961).

[14] R. Dvorak, On the unsteady boundary layer-shock wave interaction in the lower transonic region, in *Fluid Dynamics Transactions* (Elsevier, Amsterdam, 1965), pp. 63–74.

[15] E. Garnier and S. Deck, Large-eddy simulation of transonic buffet over a supercritical airfoil, in *Notes on Numerical Fluid Mechanics and Multidisciplinary Design* (Springer, Berlin, 2010), Vol. 110, pp. 135–141.
[16] T. Kouchi, S. Yamaguchi, S. Koike, T. Nakajima, M. Sato, H. Kanda, and S. Yanase, Wavelet analysis of transonic buffet on a two-dimensional airfoil with vortex generators, Exp. Fluids **57**, 1 (2016).
[17] Y. Fukushima and S. Kawai, Wall-modeled large-eddy simulation of transonic buffet over a supercritical airfoil at high Reynolds number, in *55th AIAA Aerospace Sciences Meeting*, January (American Institute of Aeronautics and Astronautics, Reston, VA, 2017), pp. 1–10.
[18] J. D. Crouch, A. Garbaruk, and D. Magidov, Predicting the onset of flow unsteadiness based on global instability, J. Comput. Phys. **224**, 924 (2007).
[19] F. Sartor, C. Mettot, and D. Sipp, Stability, receptivity, and sensitivity analyses of buffeting transonic flow over a profile, AIAA J. **53**, 1980 (2015).
[20] S. Timme, Global instability of wing shock-buffet onset, J. Fluid Mech. **885**, A37 (2020).
[21] V. Brunet, in *Advances in Hybrid RANS-LES Modelling*, edited by S.-H. Peng and W. Haase, Notes on Numerical Fluid Mechanics and Multidisciplinary Design Vol. 97 (Springer, Berlin, 2008).
[22] M. Iovnovich and D. E. Raveh, Numerical study of shock buffet on three-dimensional wings, AIAA J. **53**, 449 (2015).
[23] F. Sartor and S. Timme, Mach number effects on buffeting flow on a half wing-body configuration, Int. J. Numer. Methods Heat Fluid Flow **26**, 2066 (2016).
[24] L. Masini, S. Timme, and A. J. Peace, Analysis of a civil aircraft wing transonic shock buffet experiment, J. Fluid Mech. **884**, A1 (2020).
[25] E. Paladini, S. Beneddine, J. Dandois, D. Sipp, and J.-C. Robinet, Transonic buffet instability: From two-dimensional airfoils to three-dimensional swept wings, Phys. Rev. Fluids **4**, 103906 (2019).
[26] J. B. Dor, A. Mignosi, A. Seraudie, and B. Benoit, Wind tunnel studies of natural shock wave - Separation instabilities for transonic airfoil tests, in *Symposium Transsonicum III* (Springer, Berlin, 1989), pp. 417–427.
[27] D. G. Mabey, Beyond the buffet boundary, Aeronaut. J. **77**, 201 (1973).
[28] R. Bur, V. Brion, and P. Molton, An overview of recent experimental studies conducted in Onera S3Ch transonic wind tunnel, in *29th Congress of the International Council of the Aeronautical Sciences*, ICAS (2014).
[29] J. Dandois, Experimental study of transonic buffet phenomenon on a 3D swept wing, Phys. Fluids **28**, 016101 (2016).
[30] V. Brion, J. Dandois, R. Mayer, P. Reijasse, T. Lutz, and L. Jacquin, Laminar buffet and flow control, Proc. Inst. Mech. Eng., Part G **234**, 124 (2019).
[31] R. Placek and P. Ruchała, The flow separation development analysis in subsonic and transonic flow regime of the laminar airfoil, Transp. Res. Procedia **29**, 323 (2018).
[32] T. Davidson, Effect of incoming boundary layer state on flow development downstream of normal shock wave–boundary layer interactions, Ph.D. thesis, University of Cambridge, 2016.
[33] F. Grossi, Physics and modeling of unsteady shock wave/boundary layer interactions over transonic airfoils by numerical simulation, Ph.D. thesis, Institut National Polytechnique de Toulouse, 2014.
[34] D. Szubert, I. Asproulias, F. Grossi, R. Duvigneau, Y. Hoarau, and M. Braza, Numerical study of the turbulent transonic interaction and transition location effect involving optimisation around a supercritical airfoil, Eur. J. Mech., B: Fluids **55**, 380 (2016).
[35] J. Sznajder and T. Kwiatkowski, Analysis of effects of shape and location of micro-turbulators on unsteady shockwave-boundary layer interactions in transonic flow, J. KONES Powertrain Transp. **23**, 373 (2016).
[36] A. Memmolo, M. Bernardini, and S. Pirozzoli, Scrutiny of buffet mechanisms in transonic flow, Int. J. Numer. Methods Heat Fluid Flow **28**, 1031 (2016).
[37] M. Zauner, N. De Tullio, and N. D. Sandham, Direct numerical simulations of transonic flow around an airfoil at moderate Reynolds numbers, AIAA J. **57**, 597 (2019).
[38] M. Zauner and N. D. Sandham, Modal analysis of a laminar-flow airfoil under buffet conditions at Re=500,000, Flow, Turbul. Combust. **104**, 509 (2019).
[39] R. Vinuesa, S. M. Hosseini, A. Hanifi, D. S. Henningson, and P. Schlatter, Pressure-gradient turbulent boundary layers developing around a wing section, Flow, Turbul. Combust. **99**, 613 (2017).

[40] S. Deck, Numerical simulation of transonic buffet over an airfoil, AIAA J. **43**, 1556 (2005).
[41] J. Dandois, I. Mary, and V. Brion, Large-eddy simulation of laminar transonic buffet, J. Fluid Mech. **850**, 156 (2018).
[42] M. Zauner and N. D. Sandham, LES study of the three-dimensional behaviour of unswept wing sections at buffet conditions, in *Direct and Large-Eddy Simulation XII* (Springer, Berlin, 2019).
[43] N. A. Adams and S. Hickel, *Implicit Large-Eddy Simulation: Theory and Application* (Springer, Berlin, 2009), pp. 743–750.
[44] A. Aspden, N. Nikiforakis, S. Dalziel, and J. Bell, Analysis of implicit LES methods, Commun. Appl. Math. Comput. Sci. **3**, 103 (2008).
[45] A. Sansica, Stability and unsteadiness of transitional shock-wave/boundary-layer interactions in supersonic flows, Ph.D. thesis, University of Southampton, 2015.
[46] N. De Tullio and N. D. Sandham, Direct numerical simulations and modal analysis of subsonic flow over swept airfoil sections, arXiv:1901.04727.
[47] L. E. Jones, Numerical studies of the flow around an airfoil at low Reynolds number, Ph.D. thesis, University of Southampton, 2008.
[48] M. H. Carpenter, J. Nordström, and D. Gottlieb, A stable and conservative interface treatment of arbitrary spatial accuracy, J. Comput. Phys. **148**, 341 (1999).
[49] R. D. Sandberg and N. D. Sandham, Nonreflecting zonal characteristic boundary condition for direct numerical simulation of aerodynamic sound, AIAA J. **44**, 402 (2006).
[50] H. Sandhu and N. Sandham, Direct numerical simulation of the flow around an airfoil with unsteady wake, Tech. Rep. QMW-EP-1100, Faculty of Engineering, Queen Mary and Westfield College, University of London, 1994.
[51] M. R. Visbal and D. V. Gaitonde, On the use of higher-order finite-difference schemes on curvilinear and deforming meshes, J. Comput. Phys. **181**, 155 (2002).
[52] D. V. Gaitonde, J. S. Shang, and J. L. Young, Practical aspects of higher-order numerical schemes for wave propagation phenomena, Int. J. Numer. Methods Eng. **45**, 1849 (1999).
[53] M. R. Visbal and D. V. Gaitonde, High-order-accurate methods for complex unsteady subsonic flows, AIAA J. **37**, 1231 (1999).
[54] C. T. Jacobs, M. Zauner, N. De Tullio, S. P. Jammy, D. J. Lusher, and N. D. Sandham, An error indicator for finite difference methods using spectral techniques with application to aerofoil simulation, Comput. Fluids **168**, 67 (2018).
[55] M. Zauner, C. T. Jacobs, and N. D. Sandham, Grid refinement using spectral error indicators with application to airfoil DNS, in *ECCM-ECFD Conference*, Glasgow, 2018 (unpublished).
[56] Á. Tanarro, F. Mallor, N. Offermans, A. Peplinski, R. Vinuesa, and P. Schlatter, Enabling adaptive mesh refinement for spectral-element simulations of turbulence around wing sections, Flow, Turbul. Combust. **105**, 415 (2020).
[57] A. Sansica, N. D. Sandham, and Z. Hu, Instability and low-frequency unsteadiness in a shock-induced laminar separation bubble, J. Fluid Mech. **798**, 5 (2016).
[58] A. Lozano-Durán and J. Jiménez, Effect of the computational domain on direct simulations of turbulent channels up to $\mathrm{Re}\,\tau = 4200$, Phys. Fluids **26**, 011702 (2014).
[59] See Supplemental Material at http://link.aps.org/supplemental/10.1103/PhysRevFluids.5.083903 for an animation of the pressure gradient. See also these animations at https://youtu.be/pjRzeSYb4AY.
[60] A. Busemann, The drag problem at high supersonic speeds, J. Aeronaut. Sci. **16**, 337 (1949).
[61] M. Zauner, N. D. Sandham, A. P. S. Wheeler, and R. D. Sandberg, Linear stability prediction of vortex structures on high pressure turbine blades, Int. J. Turbomach. Propuls. Power **2**, 8 (2017).
[62] A. P. S. Wheeler, R. D. Sandberg, N. D. Sandham, R. Pichler, V. Michelassi, and G. Laskowski, Direct numerical simulations of a high-pressure turbine vane, J. Turbomach. **138**, 071003 (2016).
[63] A. K. M. F. Hussain, Coherent structures and turbulence, J. Fluid Mech. **173**, 303 (1986).
[64] W. Hu, S. Hickel, and B. van Oudheusden, Dynamics of a supersonic transitional flow over a backward-facing step, Phys. Rev. Fluids **4**, 103904 (2019).

[65] Y. Sugioka, D. Numata, K. Asai, S. Koike, K. Nakakita, and T. Nakajima, Polymer/ceramic pressure-sensitive paint with reduced roughness for unsteady measurement in transonic flow, AIAA J. **56**, 2145 (2018).
[66] A. E. Winkelman and J. B. Barlow, Flowfield model for a rectangular planform wing beyond stall, AIAA J. **18**, 1006 (1980).
[67] F. Plante and J. Dandois, Similitude between 3D cellular patterns in transonic buffet and subsonic stall, in *AIAA SciTech 2019 Forum* (AIAA, Reston, VA, 2019).
[68] H.-w. Liepmann and H. Ashkenast, Shock-wave oscillations in wind tunnels, J. Aeronaut. Sci. **14**, 295 (1947).
[69] B. Lee and L. H. Ohman, Unsteady Pressure and Force Measurements Associated with Transonic Buffeting of a Two-Dimensional Supercritical Airfoil, Tech. Rep. ADA133139 (National Aeronautical Establishment, 1983).
[70] K. Finke, Shock oscillations in transonic flows and their prevention, in *Symposium Transsonicum II* (Springer, Berlin, 1976), pp. 57–65.
[71] E. Paladini, O. Marquet, D. Sipp, J. C. Robinet, and J. Dandois, Various approaches to determine active regions in an unstable global mode: Application to transonic buffet, J. Fluid Mech. **881**, 617 (2019).
[72] https://doi.org/10.5258/SOTON/D1484.
[73] https://www.youtube.com/playlist?list=PLoPRsYcneMTKVv5XxRCReOfhQoDZ2q7GO.